Reconfigurable Three-Mode Converter for Flexible Mode Division Multiplexing Optical Networks

Mohammad Shuhrawardy, Kazi Tanvir Ahmmed, Chi Hung Yeung, Wei Jin, Liangjun He, Binghui Li, and Hau Ping Chan, *Member, IEEE*

***Abstract*—Mode converters with reconfigurable functionality are essential for enabling flexible operation in modern mode division multiplexing (MDM) technology-based optical networks. In this paper, we propose a novel reconfigurable three-mode converter capable of converting the TE_0, TE_1, and TE_2 modes to any desired output mode, such as TE_0, TE_1, or TE_2, for use in MDM optical communication system. Our device utilizes thermo-optic (TO) effects and consists of cascaded Y-junctions and Mach-Zehnder interferometers (MZIs), comprising two three-arm mode converters and one two-arm mode converter. The analytical and numerical verification of our device demonstrates its efficient operation, and the measurement results align favorably with the simulated performance. Our photonic integrated circuit (PIC) compatible fabricated device exhibits the mode conversion efficiency (MCE) of higher than 92.5% with maximum insertion loss (IL) of 8.3 dB and crosstalks (XTs) lower than −18.9 dB in the entire C band (1.530-1.565 μm). Our three-mode energy efficient and polarization-insensitive converter offers promising potential in enhancing the flexibility of MDM optical networks, making it a viable candidate for future development and deployment.**

***Index Terms*—Mode division multiplexing (MDM), flexible optical networks, capacity issue, transfer matrices, bidirectional.**

I. Introduction

In ORDER to accommodate mobile broadband networks, Big Data, Internet of Things (IoT), massive cloud computing, automated vehicles, and other broadband applications, there is a tremendous need to expand the data capacity of traditional optical networks [1], [2], [3]. MDM is regarded as the emerging and the most effective solution to address this capacity issue, along with wave length division multiplexing (WDM) [4], [5]. MDM system utilizes few-mode fiber (FMF) to carry various optical modes or mode groups where each mode is considered as an independent WDM data channel and the increased number of modes indicate increasing data capacity [6], [7], [8]. To deal with distinct modes, MDM system requires different optical devices, e.g., mode converters [9], [10], [11], mode mux-demux [12], [13], [14], mode filters [15], [16], [17], mode switches [18], [19], [20], etc., capable of handling several modes [21], [22]. Mode converter is a basic building component for MDM system [23] and improves the efficiency of optical networks and utilization of resources [9], [24]. But mode converters capable of dynamically converting a mode order to any desired order will be required for the fully flexible MDM networks [25], [26]. Moreover, optical waveguide-based photonic integrated circuit (PIC), also known as planar lightwave circuit (PLC), technology is preferable compared to bulk and fiber optics. Their popularity emerged due to their compactness, compatibility with fiber-based devices, and the ability to integrate optical (and electronic) components on a single chip [27], [28]. Over the years various PIC mode converters have been developed where the most of them are passive [29], [30], [31], [32], [33], [34], [35], [36], [37], [38], [39], [40], [41], [42], [43], [44], [45] and some have switchable operation [46], [47], [48], [49], [50], [51], [52], [53], [54]. The mode switch and converter reported in [46] and [47] support only transverse magnetic (TM) modes. The electro-optic device introduced in [48] switches between two transverse electric (TE) modes (TE_{11} and TE_{21}). The TE_0 and TE_2 modes can be converted to one another by the multi-function device stated by Kazi [49] while it is not able to handle TE_1 mode. A silicon-Sb_2S_3 hybrid materials based tunable mode converter is theoretically studied in [50]. The three-mode and four-mode converters reported in [51] and [52] are based on cascaded MMIs-MZIs and cross-connected Y-junctions, respectively. A reconfigurable mode converter using cascaded waveguide switches is demonstrated in [53]. The four-mode converter, suggested in [54], is implemented using MZI with vertically-separated arms. However, the most of the above-mentioned switchable mode converters consume relatively large power to activate the heater electrodes and are polarization-dependent. For large scale integration, also for cost effectiveness, low power optical devices are required [55]. On the other hand, polarization-independent devices are able to handle the uncertain polarization of fiber networks, eliminate the use of polarization splitter and/or polarization combiner and leverage the polarization division multiplexing (PDM) degree of freedom [56], [57], [58]. Furthermore, some of the devices possess complex structure, e.g., multilayer waveguide, inverse design, 3D composite waveguide, etc., which makes them complicated to fabricate (require multi-step lithography and/or expensive electron beam

Manuscript received 9 July 2024; accepted 11 July 2024. Date of publication 16 July 2024; date of current version 29 July 2024. This work was supported in part by the Hong Kong Innovation and Technology Commission (InnoHK Project CIMDA) and in part by the City University of Hong Kong under Project 9610543. *(Corresponding author: Hau Ping Chan.)*

Mohammad Shuhrawardy, Chi Hung Yeung, Wei Jin, Liangjun He, and Hau Ping Chan are with the Department of Electrical Engineering, City University of Hong Kong, Hong Kong (e-mail: eehpchan@cityu.edu.hk).

Kazi Tanvir Ahmmed is with the Department of Electronic Engineering, The Chinese University of Hong Kong, Hong Kong.

Binghui Li is with the Shenzhen Institute of Artificial Intelligence and Robotics for Society, The Chinese University of Hong Kong, Shenzhen 518172, China.

Digital Object Identifier 10.1109/JPHOT.2024.3428912

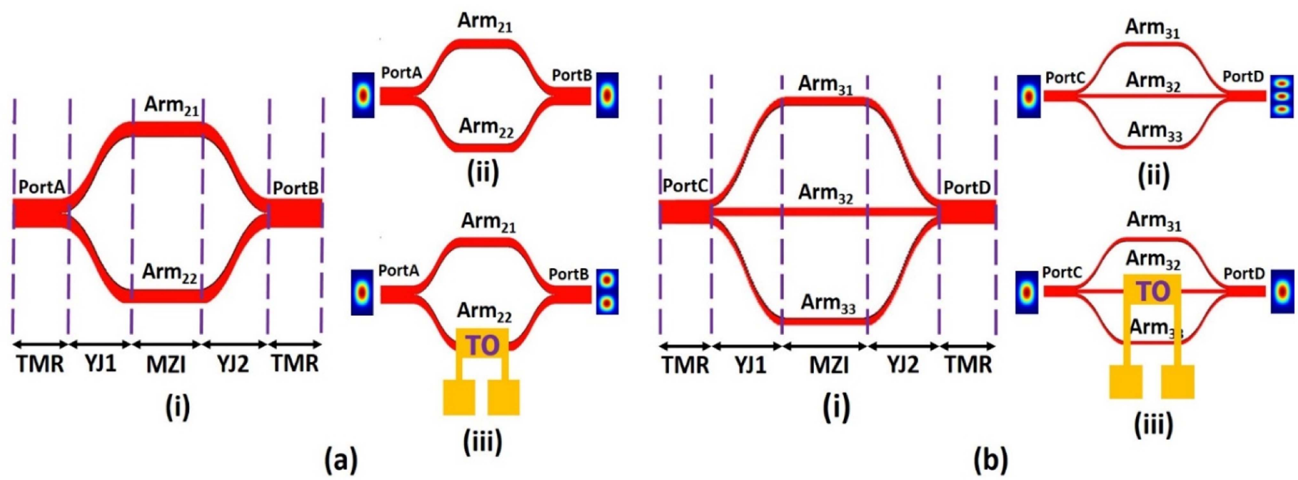

Fig. 1. (a) Operation of TWMC (i) structure of TWMC (ii) normal operation (iii) operation with TO active and (b) operation of THMC (i) structure of THMC (ii) normal operation (iii) operation with TO active.

lithography (EBL)/laser writing technique) or performing worse [58], [59].

In this article, we proposed and demonstrated a unique three-mode converter structure consisting of cascaded Y-junctions and MZIs based mode converters. The device is fabricated using traditional low-cost ultraviolet lithography (UVL) process [58]. Micro-heater electrodes are employed for controlling the phase difference of the mode array propagating along the MZI arms. MZI based Multiplexer/demultiplexer (Mux/Demux) are utilized, as in [12], for launching the single-mode inputs and getting the outputs. With such a configuration, the device can converter the three TE modes, such as fundamental mode (TE_0), first-order mode (TE_1) and second-order mode (TE_2), launched at the input port to any of the TE_0, TE_1 and TE_2 modes at the output port by tuning the ON/OFF state of the heater electrodes. Analytical validation is employed to evaluate the device operation and the simulated and experimental results support the device's performance. The measured ILs, for all various conversions of the device, are below 8.3 dB and XTs are lower than −18.9 dB with MCE more than 92.5% over the entire C band. Furthermore, the device is almost polarization-insensitive and consume relatively low power (Maximum 8.4 mW) to turn on the electrodes. Our proposed mode converter has a great opportunity to be used in fully flexible MDM optical networks.

II. Principle of Operation

The device is constructed by the integration of two-arm and three–arm mode converters (TWMC and THMC). The TWMC, (Fig. 1(a)), possesses three-mode region (TMR), two Y-junctions (YJs) and a balanced two-arm MZI where THMC, (Fig. 1(b)), composed of TMR, two YJs and an unbalanced three-arm MZI. In TWMC, the MZI possesses same path length for Arm_{21} and Arm_{22}. The MZI has equal path length for Arm_{31} and Arm_{33}, in THMC, and holds a path difference of ΔL with compare to Arm_{32} that initiates a phase difference of π [49]. For both mode converters, YJ1, MZI and YJ2 act as the power splitter, phase shifter and power combiner, respectively. TO effect is used to Arm_{22} of TWMC and Arm_{32} of THMC to originate the additional phase change required.

The operation of TWMC and THMC can be easily understood from the overall transfer matrices which are obtained from the multiplication of the transfer matrices of different parts of the converters [60], [61]. In TWMC, YJ1 is the first part and divides the launched light (fundamental or first-order mode) into two portions [62]. The output fields of the two arms are in phase and have equal magnitude for fundamental mode and holds a phase difference of 180° for first-order mode. Hence, the transfer matrices of the YJ1 of TWMC for the fundamental and first-order modes are as follows [62]:

$$\begin{bmatrix} \sqrt{1/2} \\ \sqrt{1/2} \end{bmatrix}$$

and

$$\begin{bmatrix} \sqrt{1/2} \\ -\sqrt{1/2} \end{bmatrix}$$

The second part of TWMC is the phase shifter (MZI). The transfer matrix of the two arm MZI is [60], [61]

$$\begin{bmatrix} \exp(-i\beta\Delta L) & 0 \\ 0 & \exp(-i\beta\Delta L) \end{bmatrix}$$

where β is the propagation constant and ΔL is the path difference between the arms. From multiplication of the transfer matrices, the overall transfer matrix of the TWMC is

$$P_B = \begin{bmatrix} P_{21} \\ P_{22} \end{bmatrix} = \begin{bmatrix} \exp(-i\beta\Delta L) & 0 \\ 0 & \exp(-i\beta\Delta L) \end{bmatrix} \cdot \begin{bmatrix} \sqrt{1/2} \\ \pm\sqrt{1/2} \end{bmatrix} P_A \tag{1}$$

where P_{21} and P_{22} are the e-field magnitude at the output ends of two MZI arms, P_A is the e- field magnitude at PortA and P_B is the e- field magnitude at PortB.

Now if TE_0 mode is input with no TO, it is split into two portions into the symmetric arms, Arm_{21} and Arm_{22}, with no phase change ($\beta.\Delta L = 0$). Then the transfer matrix becomes,

$$P_{B0(off)} = \begin{bmatrix} P_{21} \\ P_{22} \end{bmatrix} = \begin{bmatrix} 1 & 0 \\ 0 & 1 \end{bmatrix} . \begin{bmatrix} \sqrt{1/2} \\ \sqrt{1/2} \end{bmatrix}$$

$$P_A = \begin{bmatrix} \sqrt{1/2} \\ \sqrt{1/2} \end{bmatrix} P_A \quad (2)$$

where $P_{B0(off)}$ is the e-field magnitude at PortB when fundamental mode is launched with no TO. Equation (2) indicates that there is no mode conversion for fundamental mode when TO remains inactive (Fig. 1(a)(ii)).

When TE_0 mode is input with TO on, a phase change of π ($\beta.\Delta L = \pi$) is introduced to the Arm_{22}. Then the transfer matrix becomes

$$P_{B0(on)} = \begin{bmatrix} P_{21} \\ P_{22} \end{bmatrix} = \begin{bmatrix} 1 & 0 \\ 0 & -1 \end{bmatrix} . \begin{bmatrix} \sqrt{1/2} \\ \sqrt{1/2} \end{bmatrix}$$

$$P_A = \begin{bmatrix} \sqrt{1/2} \\ -\sqrt{1/2} \end{bmatrix} P_A \quad (3)$$

where $P_{B0(on)}$ is the e-field magnitude at PortB when fundamental mode is launched with TO turned on. Equation (3) shows a TE_0 to TE_1 mode conversion for TO in activated state (Fig. 1(a)(iii)).

Similarly, for TE_1 mode with heater off and on, the transfer matrices are as follows:

$$P_{B1(off)} = \begin{bmatrix} P_{21} \\ P_{22} \end{bmatrix} = \begin{bmatrix} \sqrt{1/2} \\ -\sqrt{1/2} \end{bmatrix} P_A \quad (4)$$

and

$$P_{B1(on)} = \begin{bmatrix} P_{21} \\ P_{22} \end{bmatrix} = \begin{bmatrix} \sqrt{1/2} \\ \sqrt{1/2} \end{bmatrix} P_A \quad (5)$$

where $P_{B1(off)}$ *and* $P_{B1(on)}$ are the e-field magnitude at PortB when first-order mode is launched with TO turned off and on, respectively.

On the other hand, following the same procedure [62], the transfer matrices of the YJ1 of THMC for the fundamental and second-order modes are

$$\begin{bmatrix} \sqrt{1/3} \\ \sqrt{1/3} \\ \sqrt{1/3} \end{bmatrix}$$

and

$$\begin{bmatrix} -\sqrt{1/3} \\ \sqrt{1/3} \\ -\sqrt{1/3} \end{bmatrix}$$

The transfer matrix of the three-arm MZI is [60], [61]

$$\begin{bmatrix} \exp(-i\beta\Delta L) & 0 & 0 \\ 0 & \exp(-i\beta\Delta L) & 0 \\ 0 & 0 & \exp(-i\beta\Delta L) \end{bmatrix}$$

From the multiplication, the overall transfer matrix of THMC is as follows:

$$P_D = \begin{bmatrix} P_{31} \\ P_{32} \\ P_{33} \end{bmatrix}$$

$$= \begin{bmatrix} \exp(-i\beta\Delta L) & 0 & 0 \\ 0 & \exp(-i\beta\Delta L) & 0 \\ 0 & 0 & \exp(-i\beta\Delta L) \end{bmatrix} . \begin{bmatrix} \pm\sqrt{1/3} \\ \sqrt{1/3} \\ \pm\sqrt{1/3} \end{bmatrix} P_C \quad (6)$$

where $P_{31,}$ $P_{32,}$ and P_{33} are the e-field magnitude at the output end of three MZI arms, P_C is the e-field magnitude at PortC and P_D is the e-field magnitude at PortD.

Then for TE_0 mode with no TO, each of Arm_{31} and Arm_{33} has a phase difference of π ($\beta.\Delta L = \pi$) with Arm_{32} and the transfer matrix becomes

$$P_{D0(off)} = \begin{bmatrix} P_{31} \\ P_{32} \\ P_{33} \end{bmatrix} = \begin{bmatrix} -1 & 0 & 0 \\ 0 & 1 & 0 \\ 0 & 0 & -1 \end{bmatrix}$$

$$. \begin{bmatrix} \sqrt{1/3} \\ \sqrt{1/3} \\ \sqrt{1/3} \end{bmatrix} P_C = \begin{bmatrix} -\sqrt{1/3} \\ \sqrt{1/3} \\ -\sqrt{1/3} \end{bmatrix} P_C \quad (7)$$

where $P_{D0(off)}$ is the e-field magnitude at PortD when fundamental mode is launched with TO off. Equation (7) indicates that there occurs TE_0 to TE_2 mode conversion for fundamental mode when TO remains inactive (Fig. 1(b)(ii)).

When TO is on for TE_0, an additional phase difference of π is originated into the Arm_{32} and now there is no phase difference ($\beta.\Delta L = 0$) among the arms. The transfer matrix becomes

$$P_{D0(on)} = \begin{bmatrix} P_{31} \\ P_{32} \\ P_{33} \end{bmatrix} = \begin{bmatrix} 1 & 0 & 0 \\ 0 & 1 & 0 \\ 0 & 0 & 1 \end{bmatrix} . \begin{bmatrix} \sqrt{1/3} \\ \sqrt{1/3} \\ \sqrt{1/3} \end{bmatrix}$$

$$P_C = \begin{bmatrix} \sqrt{1/3} \\ \sqrt{1/3} \\ \sqrt{1/3} \end{bmatrix} P_C \quad (8)$$

where $P_{D0(on)}$ is the e-field magnitude at PortD when fundamental mode is launched with TO active. Equation (8) indicates that there is no mode conversion for fundamental mode when TO is activated (Fig. 1(b)(iii)).

Similarly, for TE_2 mode with heater off and on, the transfer matrices are as follows:

$$P_{D2(off)} = \begin{bmatrix} P_{31} \\ P_{32} \\ P_{33} \end{bmatrix} = \begin{bmatrix} -1 & 0 & 0 \\ 0 & 1 & 0 \\ 0 & 0 & -1 \end{bmatrix}$$

$$. \begin{bmatrix} -\sqrt{1/3} \\ \sqrt{1/3} \\ -\sqrt{1/3} \end{bmatrix} P_C = \begin{bmatrix} \sqrt{1/3} \\ \sqrt{1/3} \\ \sqrt{1/3} \end{bmatrix} P_C \quad (9)$$

and

$$P_{D2(on)} = \begin{bmatrix} P_{31} \\ P_{32} \\ P_{33} \end{bmatrix} = \begin{bmatrix} 1 & 0 & 0 \\ 0 & 1 & 0 \\ 0 & 0 & 1 \end{bmatrix} . \begin{bmatrix} -\sqrt{1/3} \\ \sqrt{1/3} \\ -\sqrt{1/3} \end{bmatrix} P_C$$

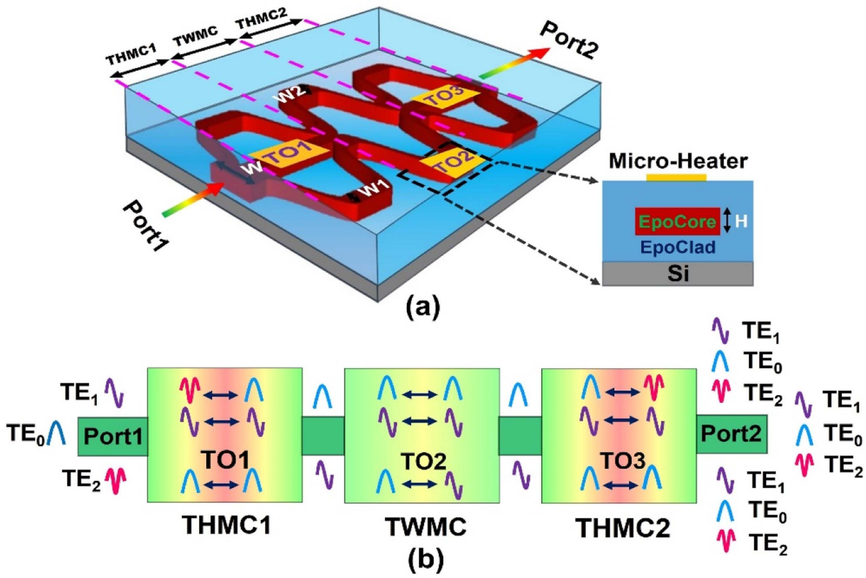

Fig. 2. Proposed reconfigurable mode converter. (a) Device structure and (b) schematic diagram.

$$= \begin{bmatrix} -\sqrt{1/3} \\ \sqrt{1/3} \\ -\sqrt{1/3} \end{bmatrix} P_C \qquad (10)$$

where $P_{D2(off)}$ *and* $P_{D2(on)}$ are the e-field magnitude at PortD when second-order mode is launched with TO turned off and on, respectively.

III. Device Structure and Function

The structure and schematic diagram of the reconfigurable mode converter are illustrated in Fig. 2. The device consists of two bidirectional THMCs (THMC1 and THMC2) sandwiched by a TWMC. The middle arm of THMC1 and THMC2 is equipped with heater electrodes TO1 and TO3, respectively, while the bottom arm of TWMC has heater electrode TO2. THMCs convert the fundamental mode (TE_0) to the second-order mode (TE_2) and reciprocal, while the first-order mode (TE_1) remains unchanged. TWMC is also reciprocal and allows the TE_0 and TE_1 modes to pass through it directly when input at any of its ends. When TO1 and TO3 are activated, THMC1 and THMC2, respectively, allow the TE_0 and TE_2 modes to pass through them without any mode conversion. By turning ON TO2, TWMC converts TE_0 to TE_1 and vice versa. THMC1 is operated in such a way that no TE_2 mode is generated at its output port. With this configuration, the device can convert among TE_0, TE_1, and TE_2 modes.

For example, we consider TE_0 to TE_1 mode conversion. TE_0 mode is launched at the input Port1 and approaches to the input stem of THMC1. Then TO1 is turned ON and hence, there is no mode conversion by THMC1 and TE_0 comes out of it and reaches to the input stem of TWMC. Now, TO2 is activated and hence, a TE_0 to TE_1 mode conversation occurs by TWMC. TE_1 mode comes to the input stem of THMC2. In this stage, TO3 remains turned OFF and hence TE_1 mode passes directly through THMC2 and finally arrives at the output Port2. Following this procedure, our device can arbitrarily convert any of TE_0, TE_1 and TE_2 modes to any of TE_0, TE_1 and TE_2 modes.

IV. Design and Simulation Results

The proposed mode converter is designed with commercially available EpoCore and EpoClad polymer materials as the core and cladding, respectively. The height and width of the Y-junction stem are selected for supporting three modes such as TE_0, TE_1 and TE_2 modes. The arm dimension of THMC1 and THMC2 support only TE_0 mode. The stem width and height of the device are W $= 14.25\ \mu$m and H $= 4.75\ \mu$m to support three modes (Fig. 2(a)). The arm width the of THMC1 and THMC2 is $W_1 = 4.75\ \mu$m and that of the TWMC is $W_2 = 7.125\ \mu$m. The branch separation angles of the Y-junctions for the THMCs and TWMC are set to 0.8° and 0.88°, respectively, to minimize excess loss. S-bends are used to design the Y-junctions so that there is sufficient arms separation for fabrication tolerance. Each MZI arm of the THMCs has a length of 2000 μm and that for TWMCs is 1500 μm which is enough to introduce the heater electrodes. The device has a total length of 17.35 mm which could be reduced significantly using SOI (silicon-on-insulator) or LNOI (lithium niobate on insulator) based high-index-contrast materials [63].

The device operation can be easily understood by monitoring the mode positions along the propagation direction. Fig. 3 illustrates the scenario where the TE_0 mode is input at Port1, and any of the TE_0, TE_1, and TE_2 modes can be observed at Port2.

For our device, the TO effect is observed by the introduction of thermo-optic coefficient of -8×10^{-5}/°C of the polymer material [49]. For a phase change of π at any MZI branch of THMCs, a temperature change of $\sim$7 °C is needed and that for TWMC the temperature change is $\sim$8.25 °C. The different mode conversion functionalities of the device are summarized in Table I.

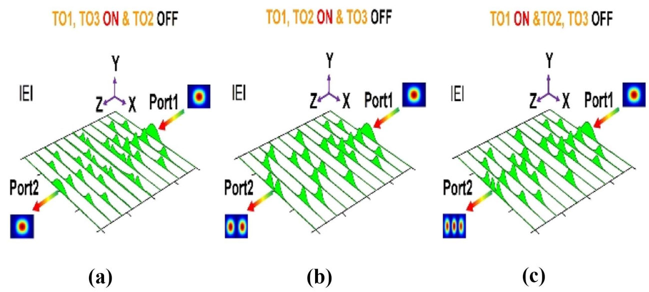

Fig. 3. Evolution of mode electric field (|E|) profile at the different positions of light propagation through the device when TE_0 is inputted. (a) TE_0 to TE_0, (b) TE_0 to TE_1 and (c) TE_0 to TE_2.

TABLE I
VARIOUS (TE) MODE CONVERSION FUNCTIONALITIES OF THE TO BASED MZI DEVICE

Input (Port1)	Heater Electrodes			Output (Port2)
	TO1	TO2	TO3	
TE_0	ON	OFF	ON	TE_0
	ON	ON	OFF	TE_1
	ON	OFF	OFF	TE_2
TE_1	OFF	ON	ON	TE_0
	OFF	OFF	OFF	TE_1
	OFF	ON	OFF	TE_2
TE_2	OFF	OFF	ON	TE_0
	OFF	ON	OFF	TE_1
	OFF	OFF	OFF	TE_2

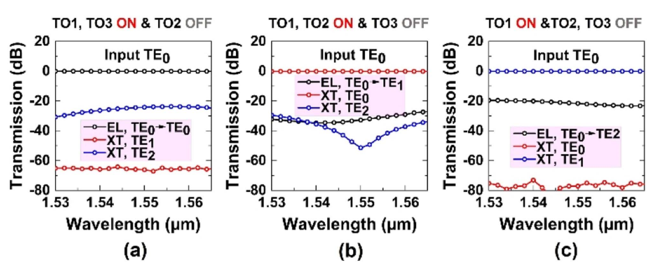

Fig. 4. Mode conversion simulated results for TE_0 input. (a) TE_0 to TE_0, (b) TE_0 to TE_1 and (c) TE_0 to TE_2.

We investigate the simulation results for the evaluation of the device performance. In simulation results, the material loss is not included. Fig. 4 shows the transmission characteristics (normalized) when TE_0 mode is input at Port1 and any of TE_0, TE_1 and TE_2 modes is output from Port2. In this case, the excess loss (EL) is between 0.06 dB and 0.13 dB over the whole C band with MCE of 97.07% to 99.01% (by deduction of EL). The EL is high for conversion of TE_0 mode to TE_2 mode and this is reasonable because higher-order modes are prone to bends and radiation loss. The XTs, at the wavelength of 1.55 μm, are between −21.68 dB and −77.10 dB and between −19.52 dB and −83.91 dB over the entire C band for all conversions of TE_0 mode.

Figs. 5 and 6 depicts the simulation results for conversion of TE_1 and TE_2 modes to TE_0, TE_1 and TE_2, respectively. From

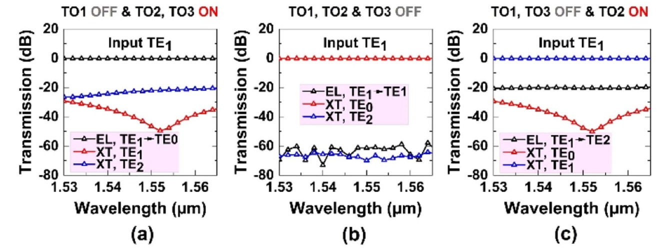

Fig. 5. Mode conversion simulated results for TE_1 input. (a) TE_1 to TE_0, (b) TE_1 to TE_1 and (c) TE_1 to TE_2.

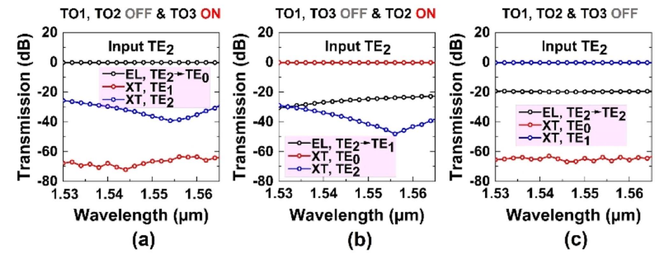

Fig. 6. Mode conversion simulated results for TE_2 input. (a) TE_2 to TE_0, (b) TE_2 to TE_1 and (c) TE_2 to TE_2.

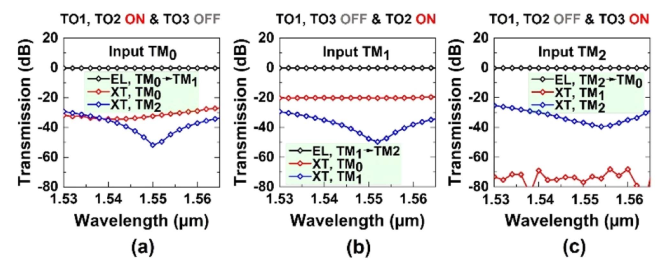

Fig. 7. Mode conversion simulated results for (a) TM_0 to TM_1, (b) TM_1 to TM_2 and (c) TM_2 to TM_0.

Fig. 5, the TE_1 mode conversion possesses the highest EL of 0.15 dB with MCE of 96.59%. The XTs are below −19.76 dB for the whole C band. For the conversion of TE_2 mode (Fig. 6), the EL is lower than 0.19 dB with MCE >95.82%. The XTs are below −19.23 dB in the entire C band. The full-vector simulation, for three TM modes, namely fundamental mode (TM_0), first-order mode (TM_1) and second-order mode (TM_2), exhibits almost the same performance as that of TE modes which confirms the negligible polarization dependency of the device. The simulation results for TM_0 to TM_1, TM_1 to TM_2 and TM_2 to TM_0 are presented in Fig. 7. For all three TM mode conversions, the ELs are between 0.10 dB and 0.15 dB and XTs stay in the range of −19.43 dB to −87. 56 dB with MCE above 96.51% in the entire C band.

V. FABRICATION AND CHARACTERIZATION

We experimentally demonstrated our device in polymer materials to take advantage of their ease of processing and reproduction, outstanding thermo-optic property, index compatibility with traditional fiber, and simple coupling [64], [65]. Commercially available polymer materials EpoCore and EpoClad

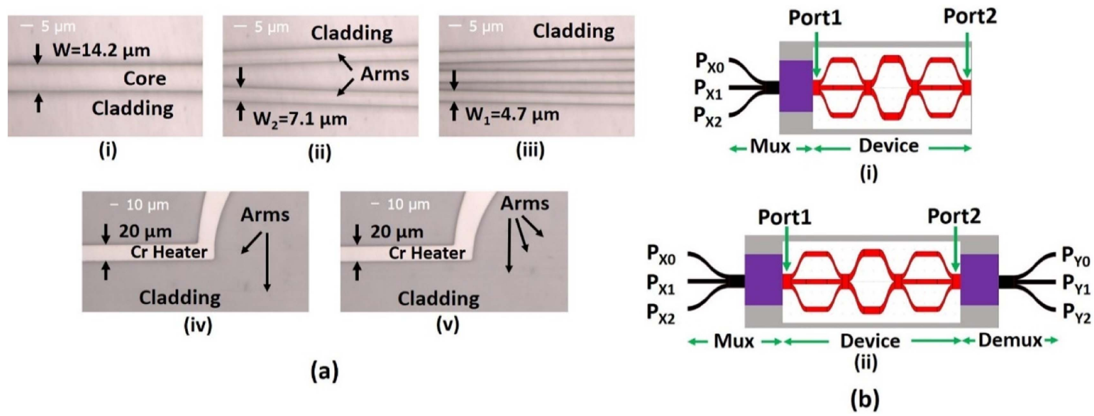

Fig. 8. (a) Microscopic images of our demonstrated device (i) three-mode section, (ii) Y-junction for TWMC, (iii) Y-junction for THMC, (iv) Cr electrode on TWMC, (v) Cr electrode on THMC and (b) schematic diagram for (i) observation of mode field patterns and (ii) transmission characteristics.

(Micro Resist Technology GmbH) was used as the core and cladding materials, respectively, to fabricate the device. The measured refractive indices of EpoCore and EpoClad with a prism coupler for TE polarization at 1.536 μm were 1.569 and 1.559, respectively. The device was fabricated in the cleanroom facilities using conventional microfabrication technology. A thin layer ($\sim$100 nm) of Chromium (Cr) was introduced as the metal electrode on top of the device. For THMCs, the length of the electrode was 2000 μm and that for TWMC was 1500 μm and the same width of 20 μm was used for both type of converters. Fig. 8(a) shows the microscopic images of different portions of the device.

For observing mode field patterns, light of the desired wavelength from a tunable laser source (81940A, Keysight Technology) was launched into the single-mode waveguide of the Mux [12] (P_{X0}, P_{X1}, and P_{X2}), Fig. 8(b)(i), using a single-mode fiber connected to the source. The Mux and the device propagated the coupled light through it and the output light was focused to the camera by an objective lens. Four heater probes with micro-positioners were used to provide the electric power to the Cr electrodes for activation of the TO effects. The polarization (TE or TM) was controlled through the adjustment of a polarization controller and a polarizer at the input and output terminals, respectively. For capturing the observed mode field patterns on the computer screen, a CCD camera (C10633, Hamamatsu Photonics) was used. The different TE mode field patterns observed from our fabricated device at different TO conditions are shown in Table II. The required electric power to turn on TO1, TO2 and TO3 electrodes are 6.7 mW, 8.4 mW and 6.6 mW, respectively. The response time of our device is less than 1.62 ms. All observed TE mode patterns adequately follow the simulation performance listed in Table I.

For further characterization, we evaluated the C-band wavelength dependency of the device. In that case, the light was launched into the Mux [12] inputs (P_{X0}, P_{X1}, and P_{X2}) and the output power was measured from the Demux [12] outputs (P_{Y0}, P_{Y1}, and P_{Y2}), Fig. 8(b)(ii), by a power meter (Newport 2832-C). The measured transmission characteristics (normalized to input) are shown in Figs. 9, 10, and 11 for the launched TE_0, TE_1 and

TABLE II
OBSERVED (TE) MODE FIELD PATTERNS (AT PORT2) OF THE PROPOSED DEVICE

Input Ports	Heater Electrodes			Output (Port2)		
	TO1	TO2	TO3	1.53 µm	1.55 µm	1.565 µm
P_{X0} (TE_0)	ON	OFF	ON			
	ON	ON	OFF			
	ON	OFF	OFF			
P_{X1} (TE_1)	OFF	ON	ON			
	OFF	OFF	OFF			
	OFF	ON	OFF			
P_{X2} (TE_2)	OFF	OFF	ON			
	OFF	ON	OFF			
	OFF	OFF	OFF			

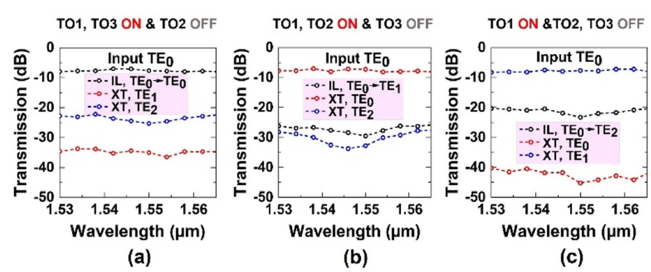

Fig. 9. Measured transmission results for TE_0 input. (a) TE_0 to TE_0, (b) TE_0 to TE_1 and (c) TE_0 to TE_2.

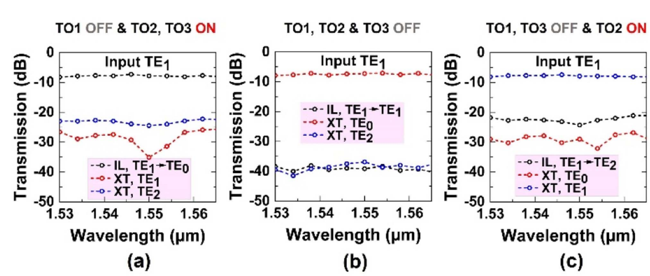

Fig. 10. Measured transmission results for TE_1 input. (a) TE_1 to TE_0, (b) TE_1 to TE_1 and (c) TE_1 to TE_2.

TABLE III
MODE FIELD PATTERNS (TE) OBSERVED AT DEMUX END OF THE DEVICE

Input Ports	Heater Electrodes			Output Ports		
	TO1	TO2	TO3	1.530 µm: P_{Y0} (TE_0), P_{Y1} (TE_1), P_{Y2} (TE_2)	1.550 µm: P_{Y01} (TE_0), P_{Y1} (TE_1), P_{Y2} (TE_2)	1.565 µm: P_{Y0} (TE_0), P_{Y1} (TE_1), P_{Y2} (TE_2)
P_{X0} (TE_0)	ON	OFF	ON			
	ON	ON	OFF			
	ON	OFF	OFF			
P_{X1} (TE_1)	OFF	ON	ON			
	OFF	OFF	OFF			
	OFF	ON	OFF			
P_{X2} (TE_2)	OFF	OFF	ON			
	OFF	ON	OFF			
	OFF	OFF	OFF			

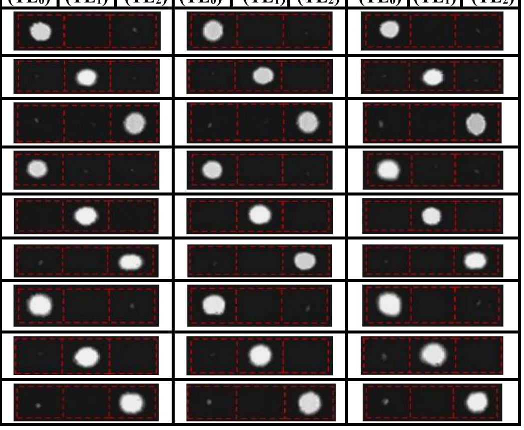

TABLE IV
COMPARISON OF OUR DEVICE WITH RECENTLY PUBLISHED WORKS

Ref.	Dynamic Operation	Polarization Insensitivity	Mode Conversion	Max. Power	Max. XT and/or Min. MCE (C band)	Material Platform and Fabrication Cost
[35]	No	Weakly sensitive	LP_{01} to LP_{11a} or LP_{01} to LP_{11b}	-	90%	Polymer/ Low (UVL)
[39]	No	No	TE_0 to TE_1 or TE_0 to TE_2	-	-6.3 dB	SOI/High (EBL)
[40]	No	No	TE_{00} or TE_{10}	-	82.6% (-0.830 dB)	SOI/ High (EBL)
[43]	No	No	E_{00} to E_{20}	-	67% (-1.741 dB)	Theoretical study
[44]	No	No	LP_{01} to LP_{11a} or LP_{01} to LP_{11b}	-	89.2%	CWG*/Medium (FsLDW**)
[49]	Yes	Yes	Between TE_0 (TM_0) to TE_2 (TM_2)	7.66 mW	-	Polymer/Low (UVL)
[50]	Yes	No	Between TE_0 and TE_1	-	-	Theoretical study
[51]	Yes	No	Among TE_0, TE_1 and TE_2	106.69 mW	−14.3 dB	SOI/High (EBL)
[52]	Yes	No	Among first four TE modes	75 mW	−16.6 dB	SOI/High (EBL)
[53]	Yes	No	Among first three TE modes	16.6 mW	−13.0 dB	SOI/High (EBL)
[54]	Yes	Yes	Among four LP modes (TE/TM)	10.5 mW	96.5% (1.55µm)	Polymer/Low or Medium (multi-step UVL or FsLDW)
Our work	Yes	Yes	Among first three modes (TE/TM)	8.4 mW	−18.9 dB/92.5%	Polymer/Low (UVL)

*Composite waveguide (CWG), **Femtosecond laser direct writing (FsLDW)

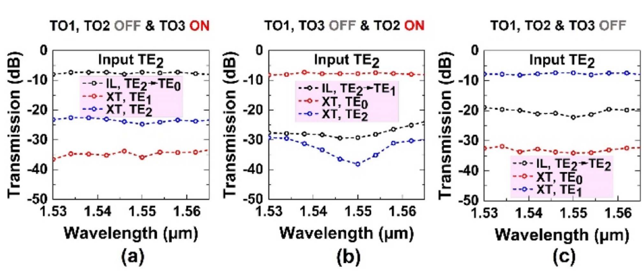

Fig. 11. Measured transmission results for TE_2 input. (a) TE_2 to TE_0, (b) TE_2 to TE_1 and (c) TE_2 to TE_2.

TE_2 modes, respectively. All power is calculated only for our device by deducting the losses of the Mux and Demux [12].

From Fig. 9(a), for TE_0 to TE_0 transmission, the IL is between 7.1 dB and 8.0 dB over the whole C band. The XTs are between −33.8 dB and −36.5 dB and between −22.3 dB and −25.3 dB for TE_1 and TE_2 modes, respectively, with MCE higher than 96.2%. At 1.55 μm, the XTs are below −25.3 dB and MCE is upper than 98.1%. The IL is in the range of 7.0 dB to 8.2 dB for TE_0 to TE_1 mode conversion in the entire C band (Fig. 9(b)). The XTs lies below −25.7 dB and MCE is >97.2% for C band while XTs are less than −29.1 dB with MCE 99.1% at 1.55 μm. From Fig. 9(c), TE_0 to TE_2 mode conversion, the IL is between 7.2 dB and 8.3 dB in the entire C band. The XTs are lower than −20.3 dB and −40.2 dB for TE_0 and TE_1 mode, respectively, with MCE above 94.1%. For 1.55 μm, the XTs are <−23.3 dB and MCE is >97.3%.

For TE_1 to TE_0 mode conversion (Fig. 10(a)), the IL is below 8.2 dB in the entire C band. The XTs remain below −25.6 dB and −22.3 dB for TE_1 mode and TE_2 mode, respectively, with MCE > 94.8%. XTs are less than −24.5 dB and MCE is >97.7% at 1.55 μm. For other two conversions (TE_1 to TE_1 and TE_1 to TE_2), the IL is lower than 8.1 dB and the XTs are below −21.1 dB with MCE above 94.0% over the C band. For 1.55 μm, the XTs are below −24.3 dB and the MCE is >97.0%. From, Fig. 11, the IL is lower than 8.2 dB, and the XTs are below −18.9 dB and the MCE is above 92.5% for the whole C band. At 1.55 μm, the XTs are less than -22.2 dB and the MCE is $>96.6\%$. Table III shows all of the mode field patters (TE) observed at the Demux end.

For our fabricated device, the measured IL is lower than 8.3 dB for TE polarization. The IL includes the material loss (2.5 dB/cm), the fiber-to-device coupling loss at the input port (2.4 dB), and excess loss (1.6 dB). By utilizing low loss material and improving the fabrication process, the IL can be greatly reduced [66], [64]. The simulated and experimental results of the device verify the mode conversion functionalities of our proposed device. A comparison of our device with recently published ones are show in Table IV.

From the Table, it is obvious that although two designs, [52] and [54], support more (four) modes, our three-mode converter consume relatively less power except [49] which can convert only between TE_0 (TM_0) and TE_2 (TM_2) modes and unable to deal with TE_1 (TM_1) mode. Our device is also almost polarization-independent which eliminate the need of polarization splitter/combiner and can be applied in PDM system [57], [58]. Furthermore, the device possess simple structure and hence conventional low cost UVL is enough to fabricate it [58], [59].

VI. Conclusion

We presented a reconfigurable three-mode converter for the MDM optical networks that can convert among any of TE_0, TE_1, and TE_2 modes by the activation or deactivation of TO effects. The device operation is validated numerically and the experimental results fairly follows the simulation performance of the device. For all mode conversions, our fabricated device exhibits maximum IL of 7.9 dB and XTs of lower than –22.2 dB and MCE above 96.6% at 1.55 μm. The device consumes relatively low power and is polarization-insensitive. Our suggested mode converter can be a good fit for improving the flexibility of MDM optical networks.

References

[1] K. Nakajima, T. Matsui, K. Saito, T. Sakamoto, and N. Araki., "Space division multiplexing technology: Next generation optical communication strategy," in *Proc. ITU Kaleidoscope: ICTs Sustain. World*, 2016, pp. 1–7.

[2] K. Kim et al., "High speed and low latency passive optical network for 5G wireless systems," *J. Lightw. Technol.*, vol. 37, no. 12, pp. 2873–2882, Jun. 2019, doi: 10.1109/JLT.2018.2866805.

[3] R. Essiambre, G. Kramer, P. J. Winzer, G. J. Foschini, and B. Goebel, "Capacity limits of optical fiber networks," *J. Lightw. Technol.*, vol. 28, no. 4, pp. 662–701, Feb. 2010, doi: 10.1109/JLT.2009.2039464.

[4] Y. Liu et al., "Arbitrarily routed mode-division multiplexed photonic circuits for dense integration," *Nature Commun.*, vol. 10, no. 1, Jul. 2019, Art. no. 3263, doi: 10.1038/s41467-019-11196-8.

[5] K. Shibahara, T. Mizuno, and Y. Miyamoto, "Long-haul mode multiplexing transmission enhanced by interference cancellation techniques based on fast MIMO affine projection," *J. Lightw. Technol.*, vol. 38, no. 18, pp. 4969–4977, Sep. 2020, doi: 10.1109/JLT.2020.3001313.

[6] K. Kitayama and N. P. Diamantopoulos, "Few-mode optical fibers: Original motivation and recent progress," *IEEE Commun. Mag.*, vol. 55, no. 8, pp. 163–169, Aug. 2017, doi: 10.1109/MCOM.2017.1600876.

[7] D. Zhou, C. Sun, Y. Lai, Y. Yu, and X. Zhang, "Integrated silicon multifunctional mode-division multiplexing system," *Opt. Exp.*, vol. 27, no. 8, pp. 10798–10805, Apr. 2019, doi: 10.1364/OE.27.010798.

[8] X. Han et al., "Reconfigurable on-chip mode exchange for mode-division multiplexing optical networks," *J. Lightw. Technol.*, vol. 37, no. 3, pp. 1008–1013, Feb. 2019, doi: 10.1109/JLT.2018.2885028.

[9] L. Liu, Y. Xu, L. Wen, Y. Dong, B. Zhang, and Y. Ni, "Design of a compact silicon-based TM-polarized mode-order converter based on shallowly etched structures," *Appl. Opt.*, vol. 58, no. 33, pp. 9075–9081, Nov. 2019, doi: 10.1364/AO.58.009075.

[10] Y. Yang, K. Chen, W. Jin, and K. S. Chiang, "Widely wavelength-tunable mode converter based on polymer waveguide grating," *IEEE Photon. Technol. Lett.*, vol. 27, no. 18, pp. 1985–1988, Sep. 2015, doi: 10.1109/LPT.2015.2448793.

[11] Z. Guo, J. Xiao, S. Wu, Y. Lai, and S. Cheng, "Compact, scalable and flexible multi-mode-converting model employing subwavelength gratings," *J. Lightw. Technol.*, early access, Jul. 01, 2024, doi: 10.1109/JLT.2024.3421379.

[12] K. T. Ahmmed, H. P. Chan, and B. Li, "Three-mode multiplexer and demultiplexer based on the Mach-Zehnder interferometer," *OSA Continuum*, vol. 4, no. 5, pp. 1519–1532, May 2021, doi: 10.1364/OSAC.418930.

[13] Q. Huang, Y. Wu, W. Jin, and K. S. Chiang, "Mode multiplexer with cascaded vertical asymmetric waveguide directional couplers," *J. Lightw. Technol.*, vol. 36, no. 14, pp. 2903–2911, Jul. 2018, doi: 10.1109/JLT.2018.2829143.

[14] Y. Wu and K. S. Chiang, "Ultra-broadband mode multiplexers based on three-dimensional asymmetric waveguide branches," *Opt. Lett.*, vol. 42, no. 3, pp. 407–410, Feb. 2017, doi: 10.1364/OL.42.000407.

[15] K. T. Ahmmed, H. P. Chan, and B. Li, "Broadband high-order mode pass filter based on mode conversion," *Opt. Lett.*, vol. 42, no. 18, pp. 3686–3689, Sep. 2017, doi: 10.1364/OL.42.003686.

[16] Q. Huang and K. S. Chiang, "Polarization-insensitive ultra-broadband mode filter based on a 3D graphene structure buried in an optical waveguide," *Optica*, vol. 7, no. 7, pp. 744–745, Jul. 2020, doi: 10.1364/OPTICA.396918.

[17] Q. Huang, W. Wang, W. Jin, and K. S. Chiang, "Ultra-broadband mode filter based on phase-shifted long-period grating," *IEEE Photon. Technol. Lett.*, vol. 31, no. 13, pp. 1052–1055, Jul. 2019, doi: 10.1109/LPT.2019.2917388.

[18] H. Xiao et al., "Optical mode switch based on multimode interference couplers," *J. Opt.*, vol. 19, Dec. 2016, Art. no. 025802, doi: 10.1088/2040-8986/19/2/025802.

[19] L. Jiang, Q. Huang, and K. S. Chiang, "Low-power all-optical switch based on a graphene-buried polymer waveguide Mach-Zehnder interferometer," *Opt. Exp.*, vol. 30, no. 5, pp. 6786–6797, Feb. 2022, doi: 10.1364/OE.452075.

[20] Y. Gao, X. Sun, P. Li, and D. Zhang, "Polymer mode selecting switch based on cascaded MMI couplers," *IEEE Photon. Technol. Lett.*, vol. 33, no. 3, pp. 147–150, Feb. 2021, doi: 10.1109/LPT.2021.3049414.

[21] Y. Su, Y. He, H. Chen, X. Li, and G. Li, "Perspective on mode-division multiplexing," *Appl. Phys. Lett.*, vol. 118, no. 20, May 2021, Art. no. 200502, doi: 10.1063/5.0046071.

[22] J. Du, W. Shen, J. Liu, Y. Chen, X. Chen, and Z. He, "Mode division multiplexing: From photonic integration to optical fiber transmission," *Chin. Opt. Lett.*, vol. 19, no. 9, 2021, Art. no. 091301, doi: 10.1364/COL.19.091301.

[23] W. Shen et al., "Chalcogenide glass photonic integration for improved 2-micron optical interconnection," *Photon. Res.*, vol. 8, no. 9, pp. 1484–1490, Sep. 2020, doi: 10.1364/PRJ.398957.

[24] H. D. T. Linh, T. C. Dung, K. Tanizawa, D. D. Thang, and N. T. Hung, "Arbitrary $TE_0/TE_1/TE_2/TE_3$ mode converter using 1×4 Y-junction and 4×4 MMI couplers," *IEEE J. Sel. Topics Quantum Electron.*, vol. 10, no. 3, Mar./Apr. 2018, Art. no. 8300708, doi: 10.1109/JSTQE.2019.2937169.

[25] Y. Yu, M. Ye, and S. Fu, "On-chip polarization controlled mode converter with capability of WDM operation," *IEEE Photon. Technol. Lett.*, vol. 27, no. 18, pp. 1957–1960, Sep. 2015, doi: 10.1109/LPT.2015.2448076.

[26] H. Xiao et al., "On-chip scalable mode-selective converter based on asymmetrical micro-racetrack resonators," *Nanophotonics*, vol. 9, no. 6, pp. 1447–1455, 2020, doi: 10.1515/nanoph-2020-0040.

[27] L. Hou and J. H. Marsh, "Photonic integrated circuits: From techniques to devices," in *Proc. Asia Commun. Photon. Conf.*, 2019, Paper S3D.3.

[28] M. Dong et al., "High-speed programmable photonic circuits in a cryogenically compatible, visible–near-infrared 200 mm CMOS architecture," *Nature Photon.*, vol. 16, no. 1, pp. 59–65, Jan. 2022, doi: 10.1038/s41566-021-00903-x.

[29] J. M. Castro, D. F. Geraghty, S. Honkanen, C. M. Greiner, D. Iazikov, and T. W. Mossberg, "Demonstration of mode conversion using anti-symmetric waveguide Bragg gratings," *Opt. Exp.*, vol. 13, no. 11, pp. 4180–4184, May 2005, doi: 10.1364/OPEX.13.004180.

[30] Y. Huang, G. Xu, and S.-T. Ho, "An ultracompact optical mode order converter," *IEEE Photon. Technol. Lett.*, vol. 18, no. 21, pp. 2281–2283, Nov. 2006, doi: 10.1109/LPT.2006.884886.

[31] D. Dai, Y. Yang, and J. E. Bowers, "Mode conversion in tapered submicron silicon ridge optical waveguides," *Opt. Exp.*, vol. 20, no. 12, pp. 13425–13439, Jun. 2012, doi: 10.1364/OE.20.013425.

[32] D. Ohana and U. Levy, "Mode conversion based on dielectric metamaterial in silicon," *Opt. Exp.*, vol. 22, no. 22, pp. 27617–27631, Oct. 2014, doi: 10.1364/OE.22.027617.

[33] D. Chen, X. Xiao, L. Wang, Y. Yu, W. Liu, and Q. Yang, "Low-loss and fabrication tolerant silicon mode-order converters based on novel compact tapers," *Opt. Exp.*, vol. 23, no. 9, pp. 11152–11159, Apr. 2015, doi: 10.1364/OE.25.014341.

[34] W. Jin and K. S. Chiang, "Mode converters based on cascaded long-period waveguide gratings," *Opt. Lett.*, vol. 41, no. 13, pp. 3130–3133, Jul. 2016, doi: 10.1364/OL.41.003130.

[35] W. Wang, J. Wu, K. Chen, W. Jin, and K. S. Chiang, "Ultra-broadband mode converters based on length-apodized long-period waveguide gratings," *Opt. Exp.*, vol. 25, no. 13, pp. 14341–14350, Jun. 2017, doi: 10.1364/OE.25.014341.

[36] H. Wang, Y. Zhang, Y. He, Q. Zhu, L. Sun, and Y. Su, "Compact silicon waveguide mode converter employing dielectric metasurface structure," *Adv. Opt. Mater.*, vol. 7, no. 4, Dec. 2018, Art. no. 1801191, doi: 10.1002/adom.201801191.

[37] H. Jia, H. Chen, J. Yang, H. Xiao, W. Chen, and Y. Tian, "Ultra-compact dual-polarization silicon mode-order converter," *Opt. Lett.*, vol. 44, no. 17, pp. 4179–4182, Aug. 2019, doi: 10.1364/OL.44.004179.

[38] Z. Cheng et al., "Sub-wavelength grating assisted mode order converter on the SOI substrate," *Opt. Exp.*, vol. 27, no. 23, pp. 34434–34441, Nov. 2019, doi: 10.1364/OE.27.034434.

[39] Y. Zhao et al., "Ultra-compact silicon mode-order converters based on dielectric slots," *Opt. Lett.*, vol. 45, no. 13, pp. 3797–3800, Jul. 2020, doi: 10.1364/OL.391748.

[40] Z. Chen, T. Lin, X. Liu, and H. Lv, "Ultra-compact broadband in-line mode converter based on a width-modulated silicon waveguide," *IEEE Photon. J.*, vol. 13, no. 2, Apr. 2021, Art. no. 2700107, doi: 10.1109/JPHOT.2021.3066198.

[41] M. M. Masnad, G. Zhang, D. Xu, Y. Grinberg, and O. Liboiron-Ladouceur, "Fabrication error tolerant broadband mode converters and their working principles," *Opt. Exp.*, vol. 30, no. 14, pp. 25817–25829, Jul. 2022, doi: 10.1364/OE.461979.

[42] Q. Huang et al., "Ultra-broadband LP_{11} mode converter with high purity based on long-period fiber grating and an integrated Y-junction," *Opt. Exp.*, vol. 30, no. 8, pp. 12751–12759, Apr. 2022, doi: 10.1364/OE.454537.

[43] Y. Zhang et al., "On-chip E_{00}–E_{20} mode converter based on multi-mode interferometer," *Micromachines*, vol. 14, no. 5, May 2023, Art. no. 1073, doi: 10.3390/mi14051073.

[44] Z. Li et al., "Three-dimensional on-chip mode converter," *Opt. Lett.*, vol. 48, no. 5, pp. 1140–1143, Mar. 2023, doi: 10.1364/OL.474307.

[45] H. Zhou et al., "Tunable on-chip mode converter enabled by inverse design," *Nanophotonics*, vol. 12, no. 6, pp. 1105–1114, Feb. 2023, doi: 10.1515/nanoph-2022-0638.

[46] W. Jin and K. S. Chiang, "Mode switch based on electro-optic long-period waveguide grating in lithium niobate," *Opt. Lett.*, vol. 40, no. 2, pp. 237–240, Jan. 2015, doi: 10.1364/OL.40.000237.

[47] W. Jin and K. S. Chiang, "Reconfigurable three-mode converter based on cascaded electro-optic long-period gratings," *IEEE J. Sel. Topics Quantum Electron.*, vol. 26, no. 5, Sep./Oct. 2020, Art. no. 4500906, doi: 10.1109/JSTQE.2020.2969568.

[48] M. Zhang, K. Chen, W. Jin, and K. S. Chiang, "Electro-optic mode switch based on lithium-niobate Mach–Zehnder interferometer," *Appl. Opt.*, vol. 55, no. 16, pp. 4418–4422, Jun. 2016, doi: 10.1364/AO.55.004418.

[49] K. T. Ahmmed, H. P. Chan, and B. Li, "Multi-function mode processing device for mode division multiplexing optical networks," *IEEE Photon. Technol. Lett.*, vol. 33, no. 2, pp. 101–104, Jan. 2021, doi: 10.1109/LPT.2020.3041627.

[50] H. Chen, T. Wang, J. Yang, and H. Jia, "Ultra-compact Sb_2S_3-silicon hybrid integrated arbitrarily cascaded tunable mode converter," *IEEE Photon. J.*, vol. 14, no. 2, Apr. 2022, Art. no. 6622407, doi: 10.1109/JPHOT.2022.3162646.

[51] X. Han et al., "On-chip non-blocking optical mode exchanger for mode-division multiplexing interconnection networks," *J. Lightw. Technol.*, vol. 39, no. 20, pp. 6563–6571, Oct. 2021, doi: 10.1109/JLT.2021.3100527.

[52] L. Lu, D. Liu, M. Yan, and M. Zhang, "On-chip reconfigurable mode converter based on cross-connected subwavelength Y-junctions," *Photon. Res.*, vol. 9, no. 1, pp. 43–48, Jan. 2021, doi: 10.1364/PRJ.402940.

[53] X. Han et al., "On-chip switchable and reconfigurable optical mode exchange device using cascaded three-waveguide-coupling switches," *Opt. Exp.*, vol. 28, no. 7, pp. 9552–9562, Mar. 2020, doi: 10.1364/OE.390164.

[54] Q. Huang, W. Jin, and K. S. Chiang, "Broadband mode switch based on a three-dimensional waveguide Mach–Zehnder interferometer," *Opt. Lett.*, vol. 42, no. 23, pp. 4877–4880, Dec. 2017, doi: 10.1364/OL.42.004877.

[55] Y. Xie et al., "Low power consumption hybrid-integrated thermo-optic switch with polymer cladding and silica waveguide core," *Polymers*, vol. 14, no. 23, Dec. 2022, Art. no. 5234, doi: 10.3390/polym14235234.

[56] S.-P. Yang, C.-H. Wu, and L. A. Wang, "Design of a polarization-insensitive and high-efficiency coplanar edge coupler for silicon photonics by using a polished conical silicon-cored-fiber," *IEEE Photon. J.*, vol. 16, no. 1, Feb. 2024, Art. no. 7100504, doi: 10.1109/JPHOT.2023.3340025.

[57] S. Han, T. J. Seok, K. Yu, N. Quack, R. S. Muller, and M. C. Wu, "Large-scale polarization-insensitive silicon photonic MEMS switches," *J. Lightw. Technol.*, vol. 36, no. 10, pp. 1824–1830, May 2018, doi: 10.1109/JLT.2018.2791502.

[58] S. Wu, X. Mu, L. Cheng, S. Mao, and H. Y. Fu, "State-of-the-art and perspectives on silicon waveguide crossings: A review," *Micromachines*, vol. 11, no. 3, Mar. 2020, Art. no. 326, doi: 10.3390/mi11030326.

[59] G. C. Righini and A. Chiappini, "Glass optical waveguides: A review of fabrication techniques," *Opt. Eng.*, vol. 54, no. 7, Jul. 2014, Art. no. 071819, doi: 10.1117/1.OE.53.7.071819.

[60] W. Y. Chan and H. P. Chan, "Two-mode mode multiplexer/demultiplexer in polymer planar waveguide," *Appl. Opt.*, vol. 53, no. 3, pp. 496–502, Jan. 2014, doi: 10.1364/AO.53.000496.

[61] G. Weihs, M. Reck, H. Weinfurter, and A. Zeilinger, "All-fiber three-path Mach-Zehnder interferometer," *Opt. Lett.*, vol. 21, no. 4, pp. 302–304, Feb. 1996, doi: 10.1364/OL.21.000302.

[62] T. Tamir, "Waveguide transitions and junctions," in *Guided-Wave Optoelectronics*, 2nd ed. Berlin, Germany: Springer, 1990, pp. 123–125.

[63] Z. Chen et al., "A universal approach to high-index-contrast flexible integrated photonics," *Adv. Opt. Mater.*, vol. 11, no. 9, 2023, Art. no. 2202824, doi: 10.1002/adom.202202824.

[64] H. Ma, A. K.-Y. Jen, and L. R. Dalton, "Polymer-based optical waveguides: Materials, processing, and devices," *Adv. Mater.*, vol. 14, no. 19, pp. 1339–1365, Oct. 2002, doi: 10.1002/1521-4095(20021002)14:19<1339::AID-ADMA1339>3.0.CO;2-O.

[65] L. Eldada and L. W. Shacklette, "Advances in polymer integrated optics," *IEEE J. Sel. Topics Quantum Electron.*, vol. 6, no. 1, pp. 54–68, Jan./Feb. 2000, doi: 10.1109/2944.826873.

[66] A. Yeniay, R. Gao, K. Takayama, R. Gao, and A. F. Garito, "Ultra-low-loss polymer waveguides," *J. Lightw. Technol.*, vol. 22, no. 1, pp. 154–158, Jan. 2004, doi: 10.1109/JLT.2003.822206.